Mechanical model of diamond wire sawing for curved surfaces

Zhiteng Xu [1,4], Xinjiang Liao [2,3], Xun Chen [4], Zhiyuan Lai [1], Hui Huang [1,2,3,*]

1. Institute of Manufacturing Engineering, Huaqiao University, Xiamen 361021, China
2. College of Mechanical Engineering and Automation, Huaqiao University, Xiamen 361021, China
3. State Key Laboratory of High-performance Tools, Huaqiao University, Xiamen 361021, China
4. Faculty of Engineering and Technology, Liverpool John Moores University, Liverpool L3 3AF, United Kingdom

*. Corresponding author. E-mail address: huanghuihh@hotmail.com (H. Huang)

Abstract:

Diamond wire sawing is effective in machining complex parts. During the wire-cutting process, the cutting force affects the wire causing different shape changes, thereby affecting the machining quality. This paper introduces a wire sawing mechanical model for curved surfaces that considers the interdependence between the spatial motion of the wire, cutting force, and material removal. A wire bow angle measurement system was built using spring displacement sensors, and the accuracy of the mechanical model was verified through curved surface cutting experiments. The mechanical model was used to analyze the influences of the machining parameters and twist surface cutting process on the wire bow angle. The results showed that the sawing twisted surface increased the float amplitude of the wire bow angle. The wire feed rate at both ends varied with time owing to the wire twisting motion. The change in the wire feed rate at both ends was the primary factor affecting the change in the wire bow angle during the twist surface-sawing process. When sawing twisted, curved surfaces, the wire bow angle gradually decreases with increasing preloading force and wire velocity and a decreasing workpiece feed rate. Increasing the wire velocity and decreasing the workpiece feed rate can reduce the float amplitude of the wire bow angle, thereby enhancing the stability of the cutting process. This study lays the theoretical groundwork for understanding wire deformation during curved surface sawing.

Keywords: Wire sawing; Curved surface; Mechanical model; Wire bow angle

Nomenclature

a_w	wire motion acceleration (m/s^2)	$s_{w,k}$	slope on the right side of the wire point $\mathbf{w}_k$
dt	time intervals (s)	spval	extract point of the B-spline interpolation function
d_w	wire diameter (mm)	spapi	B-spline interpolation function
dx	initial contact points horizontal interval (mm)	T	machining time (s)
F_n	local normal force (N)	T_s	reciprocating cycle time (s)
F_t	local tangential force (N)	$T_{L,R}$	tension on both side of the wire point $\mathbf{w}_k$ (N)
F_1	preloading force (N)	T_k	tension on the right side of wire point $\mathbf{w}_k$ (N)
k_f	Preston coefficient (mm^2/N)	v_s	wire velocity (m/s)
M	number of wire points set	v_f	workpiece feed rate (mm/min)
N	number of contact points	$v_{fL,R}$	wire feed rate at both end (mm/min)
$\mathbf{P}$	points set representing the workpiece contour	$\mathbf{W}$	wire points set
$\mathbf{p}_i$	contact points	$\mathbf{w}_k$	wire point
$\mathbf{P}_{L,R}$	control path points set on both end of the wire	α_k	angle between the horizontal axis and wire segment (°)
$\mathbf{p}_{L,Rt}$	control path points at different times	β_k	angle between the horizontal axis and tangential force (°)
$\mathbf{P}_{:1}$	x coordinates set of the contact points set $\mathbf{P}$	θ_k	angle between the tension and tangential force (°)
$\mathbf{P}_{:2:3}$	y and z coordinates set of the contact points set $\mathbf{P}$	$\theta_{bowL,R}$	wire bow angle on both side of the workpiece (°)
Q	volume of material removal (mm^3)	Δ_i	contact point displacement (mm)
$\boldsymbol{S}_W$	set of slopes for wire segment	μ	force ratio coefficient
		γ	tension ratio on both sides of the wire points $\mathbf{w}_k$

1. Introduction

The diamond wire sawing (DWS) technique, which is characterized by a low cutting temperature, minimal cutting force, superior surface quality, and precise contour accuracy, is widely used in the wafer machining of materials such as silicon [1,2], silicon carbide (SiC) [3], and sapphire [4–7]. The DWS technique was initially adopted in the 1990s [8–10]. In studies on wafer machining using diamond wire, scholars have focused on the effects of machining and wire parameters on the surface quality [11,12]. Yin et al. [13] based on the machining mechanisms of brittle material removal and surface generation to establish a mathematical model. Costa et al. [14] conducted experiments on sawing monocrystalline silicon with a loop diamond wire and analyzed the influence of machining parameters on the depth of micro-cracks. Gao et al. [15] conducted experimental and numerical analyses of the depth of subsurface crack damage during single-crystal silicon carbide sawing with a diamond wire based on finite element models. The results indicate that increasing the wire velocity and reducing the feed rate can decrease the surface crack and subsurface damage depths, thereby improving the surface quality. Li et al. [16] confirmed that the cutting force generated during wire sawing is an important factor affecting the surface quality of wafers. Therefore, to establish a numerical sawing force prediction model, Wang et al. [17] considered ductile and brittle fracture removal for each abrasive. Li et al. [18] derived an analytical cutting force model for the wire saw machining process by analyzing the forces generated from chip formation and friction of a single abrasive. In recent years, DWS has emerged as an ideal option for efficiently machining complex-shaped parts [19,20]. During the sawing process, the guide roller drives the wire to reciprocate and controls the relative movement between the workpiece and the wire to achieve cutting [21–25]. The amount of material removed during part machining is significantly reduced by forming a separation surface [26]. Consequently, this technique offers the advantages of high efficiency and minimal material waste during curved surface machining.

The mechanism of DWS involves fixed grinding, which is considered a two-body grinding process comprising a workpiece and abrasive grains fixed on a wire core [27–32]. Typical methods of fixing abrasive grains on core wires can be distinguished by resin bonding [33–38], electroplating [39–44], and brazing [45–49] according to the type of bonding mode. Its primary distinction from other abrasive machining methods is the use of a flexible wire as a tool to generate the required abrasive pressure. Consequently, the wire reacts in various shapes under the influence of the cutting force [50–54]. This factor influences the entire cutting process and profoundly affects machining quality [55–58]. The wire bow angle is commonly employed as a quantitative measure to characterize the wire deformation [59,60].

The deformation of the wire saw can be effectively analyzed by establishing a mechanical model of the cutting process. Teomete [61] modeled a wire as a flexible beam structure subjected to a uniformly distributed vertical load at the center, but completely neglected the influence of frictional forces. Zhang et al. [62] assumed that the wire was a continuum with some degree of flexibility and elasticity during cutting. They segmented the wire into differential separations for stress analysis, accounting for both horizontal and vertical forces. Qiu et al. [63] examined the wire bow resulting from the feed motion and cutting load by utilizing macroscopic mechanical conditions as the basis for their analysis. Liu et al. [64] and Li et al. [18] posited that the material removal rate (MMR) was also a primary factor that influenced wire deformation. Liedke and Kuna [65] investigated the balance between the material removal and cutting force. They devised a macroscopic mechanical model to describe the wire shape during steady-state cutting under different machining parameters. Lai et al. [66] introduced a comprehensive model to delineate the interplay between the wire shape, cutting force, and material removal. They validated the accuracy of the model through experiments involving both rocking and reciprocating wire sawing techniques.

To date, the establishment of wire deformation models for wire sawing has been limited to plane surface cutting. Compared to cutting plane surfaces, wire sawing on

curved surfaces involves more complex machining paths, resulting in constant changes in the direction and magnitude of the feed rate on both sides of the wire. Additionally, with the twisting motion, the contact length changes simultaneously. These factors affect cutting forces and material removal, leading to complex variations in the shape of the wire. Therefore, using only the mechanical model of the wire-sawing plane surface is insufficient to analyze the influence of the kinematics of curved surface sawing on the wire shape.

The remainder of this paper is organized as follows. Section 2 introduces a mechanical model of a curved wire sawing surface based on the spatial motion, sawing force, and material removal of the wire. Section 3 verifies the accuracy of the theoretical model by comparing the experimental measurements of the wire bow angle with the simulation results. Section 4 analyzes the influence of the twist surface-sawing process and machining parameters on the wire bow angle based on the established simulation model. Furthermore, it revealed the influence of the wire feed rate at both ends on the wire bow angle during the simulation machining of the twisted surface. The main conclusions are summarized in the last section (Section 5).

2. Mechanical model for wire sawing of curved surface

The process of analyzing the wire sawing of curved surfaces requires comprehensive consideration of the spatial motion, cutting force, and material removal of the wire. Therefore, models for each aspect were established, and a calculation procedure was devised to simulate the curved surface wire-cutting process. The model in this study was based on the following assumptions: 1. The tension force on the entrance side is equal to the preloading force F_1. 2. The angles between the tension and tangential force on both sides of the contact point were equal. 3. The direction of material removal was determined by the resultant normal forces in the xy and xz planes. 4. Changes in the wire diameter caused by wire wear were ignored.

2.1. Wire spatial motion

In previous mechanical analyses of the wire-sawing process, it was assumed that the wire was differentiated as a continuum to calculate the cutting force [65]. The wire deflections at different positions on the wire were calculated by considering the segmented feed distance and material removal. Finally, an integral calculation is performed based on the boundary conditions to obtain the shape of the wire. Considering that the sawing state of the wire changes continuously during curved surface cutting, defining the boundary conditions in non-steady-state wire sawing becomes overly complex. Therefore, based on the discrete approach, a wire in space is defined by a series of connected discrete point sets, as shown in **Fig. 1.** The temporal evolution of the wire shape can be expressed by the changes in the coordinates of the wire point sets.

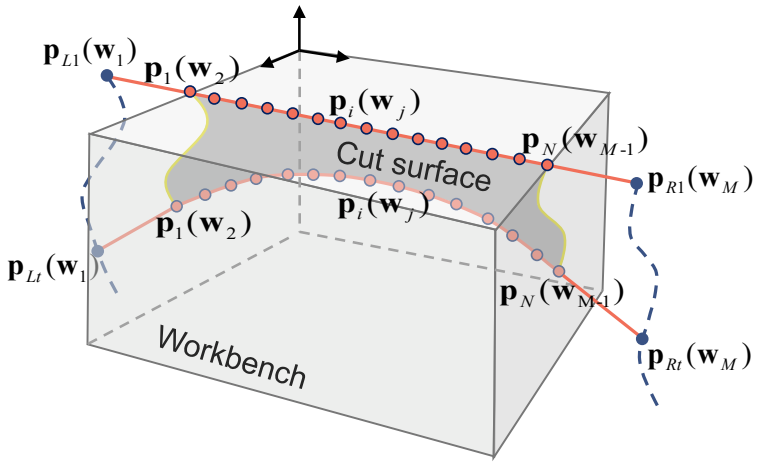

Fig. 1. Schematic diagram illustrating the spatial motion process of a wire defined by a series of connected discrete point sets. ($\mathbf{P}_{L,R}$: the control path points set on both end of the wire. **p**: the contact points between wire and workpiece. **w**: the wire points).

The world coordinate system $\boldsymbol{R} = [x, y, z]$ is established using the vertex of the workpiece as the coordinate origin. Through a kinematic analysis of the curved surface of the wire sawing, the control path points set on both sides of the wire can be obtained using **Eq. (1).**

$$\mathbf{P}_{L,R}=[\mathbf{p}_{L,R1},...,\mathbf{p}_{L,Rt},...,\mathbf{p}_{L,RT}]^{\mathrm{T}}\in\square^{T\times3},\mathbf{p}_{L,Rt}=\left[x_{L,Rt},y_{L,Rt},z_{L,Rt}\right], \quad (1)$$

where $\mathbf{P}_{L,R}$ is the control path points set on both ends of the wire; $\mathbf{p}_{L,Rt}$ is the point at different times; $x_{L,Rt}$, $y_{L,Rt}$, and $z_{L,Rt}$ are the coordinates of $\mathbf{p}_{L,Rt}$; and T is machining time.

The contact points set between the wire and workpiece are defined in **Eq. (2).**

$$\mathbf{P}=[\mathbf{p}_1,...,\mathbf{p}_i,...,\mathbf{p}_N]^{\mathrm{T}}\in\square^{N\times3},\mathbf{p}_i=[x_i,y_i,z_i], \quad (2)$$

where $\mathbf{P}$ is the contact point set between the wire and workpiece; $\mathbf{p}_i$is the contact point; x_i, y_i, and z_i are the coordinates of $\mathbf{p}_i$, and N is the number of contact points.

The wire segments that were not in contact with the workpiece were only affected by the tension force; these wire segments were straight lines and did not deform. Therefore, the wire segments of the workpiece can be defined by the control path points and the first and last contact points. Wire point set $\mathbf{W}$ can then be represented by **Eq. (3).**

$$\mathbf{W}=[\mathbf{w}_1,...,\mathbf{w}_k,...,\mathbf{w}_M]^{\mathrm{T}}=[\mathbf{p}_{Lt},\mathbf{P},\mathbf{p}_{Rt}]^{\mathrm{T}}\in\square^{M\times3},\mathbf{w}_k=[x_k,y_k,z_k], \quad (3)$$

where $\mathbf{W}$ is the wire point set; $\mathbf{w}_k$ is the wire point; x_k, y_k, and z_k are the coordinates of $\mathbf{w}_k$, and M is the number of wire points in set $\mathbf{W}$, M=N+2

2.2. Sawing force model

In the world coordinate system, the movement of the point position is equivalent to the sum of the movement vectors in the xy and xz planes. Therefore, it is reasonable to project the wire point on the xy and xz planes to build the force model and then calculate the position coordinates at the next moment.

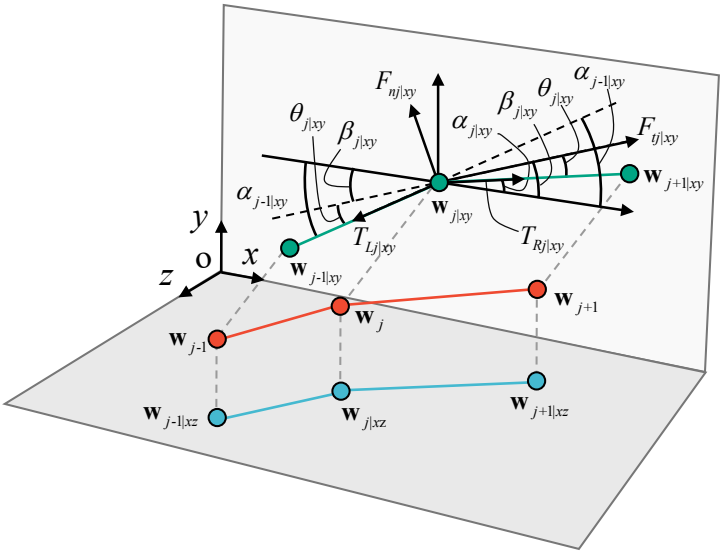

Fig. 2. Schematic diagram illustrating the force analysis of wire points projected on the xy plane (the same force analysis also applies to the xz plane).

A schematic diagram of the force analysis of wire points projected onto the xy plane is illustrated in **Fig. 2**, and the same representation applies to the xz plane. The slope of the wire segment between two adjacent wire points on the xy and xz projection planes can be calculated using **Eq. (4)**.

$$\begin{cases} \mathbf{S}_W = [\mathbf{s}_{w,1},\ldots,\mathbf{s}_{w,k},\ldots,\mathbf{s}_{w,M-1}]^{\mathrm{T}} \\ \mathbf{s}_{w,k}(1,2) = \mathbf{s}_{wxy,k} = \dfrac{\mathbf{w}_{k+1}(1,2) - \mathbf{w}_k(1,2)}{\mathbf{w}_{k+1}(1,1) - \mathbf{w}_k(1,1)}, \\ \mathbf{s}_{w,k}(1,3) = \mathbf{s}_{wxz,k} = \dfrac{\mathbf{w}_{k+1}(1,3) - \mathbf{w}_k(1,3)}{\mathbf{w}_{k+1}(1,1) - \mathbf{w}_k(1,1)} \end{cases} \tag{4}$$

where $\mathbf{S}_W$ is the set of slopes for the wire segments, and $\mathbf{s}_{w,k}$ is the slope on the right side of wire point $\mathbf{w}_k$.

The angle α_k between the horizontal axis and the wire segment is calculated using the trigonometric functions of the slope of the wire point.

$$\alpha_k = \arctan(\mathbf{s}_{w,k}) \quad \mathrm{k} = (1,\ldots,M-1)\,. \tag{5}$$

Establishing a local coordinate system with the wire point $\mathbf{w}_k$ as the origin for force analysis, the angle β_k between the horizontal axis and the tangential force is

$$\beta_k = \frac{\alpha_{k-1} + \alpha_k}{2} \quad (k = 2,...,M-1). \tag{6}$$

Assuming the angle θ_k between tension and tangential force on both sides of the contact point is equal, it is calculated as

$$\theta_k = \left|\beta_k - \alpha_k\right| = \left|\alpha_{k-1} - \beta_k\right| \quad (k = 2,...,M-1). \tag{7}$$

The mechanical equilibrium equation of the wire point is

$$\begin{cases} F_{nk} = \left(T_{Lk} + T_{Rk}\right)\sin\theta_k \\ F_{tk} = \left(T_{Lk} - T_{Rk}\right)\cos\theta_k \quad (k = 2,...,M-1), \\ F_{tk} = \mu F_{nk} \end{cases} \tag{8}$$

where F_n is the local normal force, F_t is the local tangential force, $T_{L,R}$ is the tension force on both side of the wire point $\mathbf{w}_k$, and μ is force ratio coefficient.

The tension ratio γ on both sides of the wire points is

$$\gamma_k = \frac{T_{Rk}}{T_{Lk}} = \frac{\cos\theta_k - \mu\sin\theta_k}{\cos\theta_k + \mu\sin\theta_k} \quad (k = 2,...,M-1). \tag{9}$$

At adjacent wire sawing points, the tension on the right side of the left wire point $\mathbf{w}_{k-1}$ is equal to the tension on the left side of the right wire point $\mathbf{w}_k$. Therefore, **Eq. (9)** can be rewritten as

$$\gamma_k = \frac{T_k}{T_{k-1}} = \frac{\cos\theta_k - \mu\sin\theta_k}{\cos\theta_k + \mu\sin\theta_k} \quad (k = 2,...,M-1), \tag{10}$$

where T_k is the tension on the right side of wire point $\mathbf{w}_k$.

The normal force at the wire point can be obtained using

$$F_{nk} = (T_k + T_{k-1})\sin\theta_k \quad (k = 2,...,M-1). \tag{11}$$

The tension force on the entrance side was assumed to be equal to the preloading force F_1. For example, as the wire moves from left to right, the tension acting on the right side of $\mathbf{w}_1$ is equal to the preloading force F_1. As shown in **Fig. 3**, the projected components of the preloading force on the xy and xz planes can be calculated using **Eq. (12)** according to the wire point set coordinates.

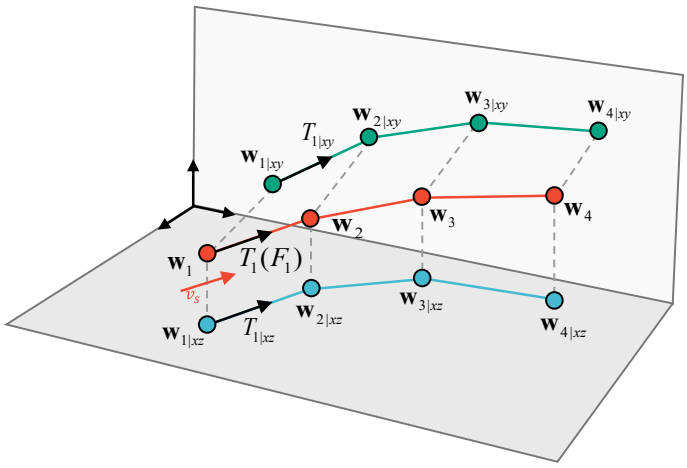

Fig. 3. Schematic diagram illustrating the projection components of the preloading force on the xy plane and xz plane (calculated based on the coordinates of the wire points).

$$\begin{aligned} T_1(1,2) = T_{1|xy} &= F_1 \times \frac{(x_2 - x_1)^2 + (y_2 - y_1)^2}{(x_2 - x_1)^2 + (y_2 - y_1)^2 + (z_2 - z_1)^2} \\ T_1(1,3) = T_{1|xz} &= F_1 \times \frac{(x_2 - x_1)^2 + (z_2 - z_1)^2}{(x_2 - x_1)^2 + (y_2 - y_1)^2 + (z_2 - z_1)^2} \end{aligned}, \tag{12}$$

where x_1, y_1, and z_1 and x_2, y_2, and z_2 are the coordinates of the first and second wire points, respectively.

The tension on the right of each wire point $\mathbf{w}_k$ can be calculated as

$$\begin{cases} T_2 = \gamma_2 \cdot T_1 \\ T_3 = \gamma_2 \cdot \gamma_3 \cdot T_1 \\ T_4 = \gamma_2 \cdot \gamma_3 \cdot \gamma_4 \cdot T_1 \\ \vdots \\ T_{M-1} = \gamma_2 \cdot \gamma_3 \cdots \gamma_{M-1} \cdot T_1 \end{cases}. \tag{13}$$

When the wire moved in the opposite direction, **Eq. (12)** and **Eq. (13)** can be rewritten as **Eq. (14)** and **Eq. (15)**.

$$\begin{aligned} T_{M-1}(1,2) = T_{M-1|xy} &= F_1 \times \frac{(x_M - x_{M-1})^2 + (y_M - y_{M-1})^2}{(x_M - x_{M-1})^2 + (y_M - y_{M-1})^2 + (z_M - z_{M-1})^2} \\ T_{M-1}(1,3) = T_{M-1|xz} &= F_1 \times \frac{(x_M - x_{M-1})^2 + (z_M - z_{M-1})^2}{(x_M - x_{M-1})^2 + (y_M - y_{M-1})^2 + (z_M - z_{M-1})^2} \end{aligned}, \tag{14}$$

where x_M, y_M, and z_M and x_{M-1}, y_{M-1}, and z_{M-1} are the coordinates of the last wire point and second-to-last wire point, respectively.

$$\begin{cases} T_1 = \gamma_2 \cdot \gamma_2 \cdots \gamma_{M-1} \cdot T_{M-1} \\ \vdots \\ T_{M-4} = \gamma_{M-3} \cdot \gamma_{M-2} \cdot \gamma_{M-1} \cdot T_{M-1} \\ T_{M-3} = \gamma_{M-2} \cdot \gamma_{M-1} \cdot T_{M-1} \\ T_{M-2} = \gamma_{M-1} \cdot T_{M-1} \end{cases} \tag{15}$$

2.3. Material removal model

In abrasive machining, the volume of material removal dQ is typically linearly related to the normal force F_n, relative velocity v_s, and machining time dt. This functional relationship is referred to as the Preston equation, and the linear coefficient is called the Preston coefficient. The volume of material removal dQ is calculated using **Eq. (16)** [67–71].

$$dQ_i = k_f F_{ni} v_s dt \,. \tag{16}$$

We assumed that the direction of material removal at the contact point was determined by the resultant force of the normal force in the xy and xz planes. The calculation of the workpiece displacement at the contact point with the wire is illustrated in **Fig. 4.**

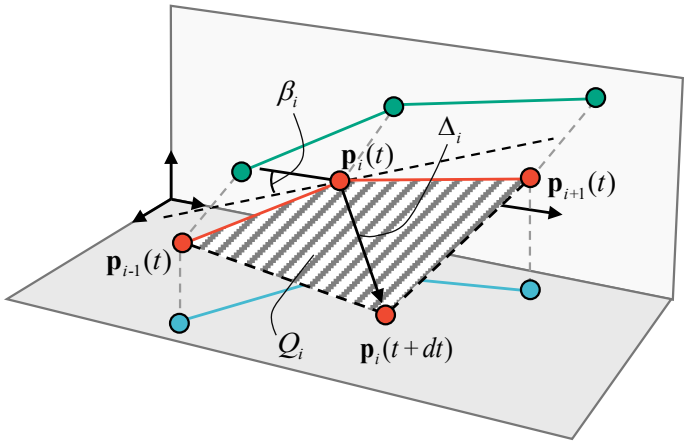

Fig. 4. Schematic diagram illustrating the calculation of contact point displacement based on material removal. (Δ_i is the contact point displacement, and Q_i is the volume of material removal).

Ignoring the change in wire diameter caused by wire wear during the cutting process, the volume of material removal dQ is equal to the area formed by the contact

point displacement Δ_i and adjacent points multiplied by the wire diameter d_w. The contact point displacement Δ_i is calculated by **Eq. (17).**

$$\Delta_i = \frac{2 \cdot dQ_i \cdot \cos\beta_i}{\left|\mathbf{p}_{i+1}(1,1) - \mathbf{p}_{i-1}(1,1)\right| \cdot d_w}. \tag{17}$$

The coordinates of the displaced contact points were fitted to obtain a curve. Compared to other fitting methods, B-spline interpolation fitting exhibits superior smoothness and flexibility, allowing for a more accurate representation of the curve. In addition, the fifth-order B-spline interpolation function provided higher fitting accuracy. Therefore, a fifth-order B-spline interpolation was used to fit the y and z coordinates of the contact points separately after displacement. The y and z coordinates of the interpolation function are extracted based on the x-coordinate of the initial contact point set. The updated coordinates of the contact point set are

$$\begin{aligned} &\mathbf{P}_{:1}(t+dt) = \mathbf{P}_{:1}(t) \\ &\mathbf{P}_{:2:3}(t+dt) = \mathrm{spval}(\mathrm{spapi}(5, \mathbf{P}_{:2:3}(t) + \Delta(t) \cdot \cos\boldsymbol{\beta}(t)), \mathbf{P}_{:1}(t)) \end{aligned}, \tag{18}$$

where $\mathbf{P}_{:1}$ is the x-coordinate set of the contact point set $\mathbf{P}$, $\mathbf{P}_{:2:3}$ is the y- and z-coordinate sets of the contact point set $\mathbf{P}$, spapi is the B-spline interpolation function, and spval is the extract point of the B-spline interpolation function.

2.4. Iterative calculation flow of curve surface sawing

A mechanical model of wire sawing on curved surfaces was constructed by iteratively calculating the spatial motion, sawing force, and material removal. The modeling methodology comprised four main steps (refer to steps (i)–(iv) in **Fig. 5**).

(i) The motion path of the wire was obtained through kinematic analysis. Based on the workpiece feed rate v_f and time interval *dt*, the wire control path point sets $\mathbf{P}_{L,R}$ in the time sequence were calculated. The initial contact points between the wire and the workpiece were determined using the horizontal interval *dx*.

(ii) According to the preloading force F_1, the force ratio coefficient μ, and the wire geometry, the normal force F_n on the contact point $\mathbf{p}_i$ between the wire and the workpiece is obtained.

(iii) Based on the normal force F_n at contact point $\mathbf{p}_i$, the contact point material removal volume Q was calculated using the Preston function. The contact point displacement Δ_i is obtained through the material removal volume Q, the area formed by adjacent points, and the wire diameter d_w.

(iv) A fifth-order B-spline interpolation function was used to fit the coordinates of the contact points after displacement. The points of the interpolation function are extracted based on the horizontal coordinates of the initial contact point set to update the set of contact points.

Finally, the completion of the calculation is determined. If not completed, return to step (ii).

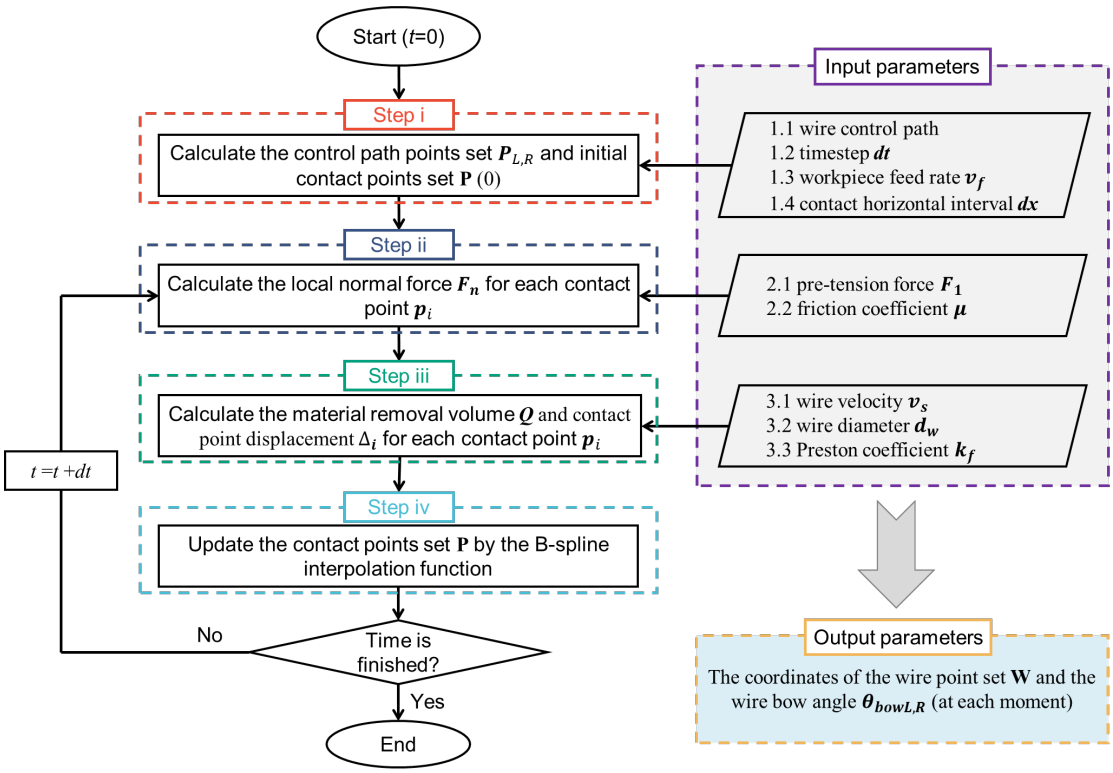

Fig. 5. Diagram illustrating the methodology of the mechanical model for wire sawing of curved surfaces (through iterative calculation of wire spatial motion, sawing force, and material removal).

3. Validation through curved surface wire-cutting experiments

The wire bow angle is commonly employed as a quantitative measure to characterize wire deformation. Therefore, a spring displacement sensor was used to build a curved wire bow measurement system to detect and record the wire bow angle during a curved surface wire-sawing experiment. The accuracy of the proposed model was verified by comparison with the values simulated using the mechanical simulation model.

3.1. Diamond wire sawing on curved surface

The experimental setup for DWS on curved surfaces is illustrated in **Fig. 6**. A single diamond wire saw machine (JXQ-1201, No. 45, Research Institute of China Electronics Technology Group Corporation) was used. During the experiment, the spatial position of the wire remained unchanged while the workpiece was mounted onto a five-axis computer numerical control (CNC) machine, allowing material removal by contacting the workpiece with the wire through movements along the X, Y, and Z axes as well as rotations around the B and C axes. The calculation in the simulation of curved surface wire sawing used inverse kinematics to obtain the control path point sets at both ends of the wire when the spatial position of the workpiece remained unchanged. The preloading force (F_1) was determined using a wire sawing machine, and a force sensor was installed on the guide wheel to provide feedback on the wire tension force. A pair of air cylinders was employed to adjust the preloading force of the wire to ensure that it remained at a set value. A transparent K9 crystal 50 mm in length was used as the experimental material. The cutting process involved two changes in the direction of the machining motion.

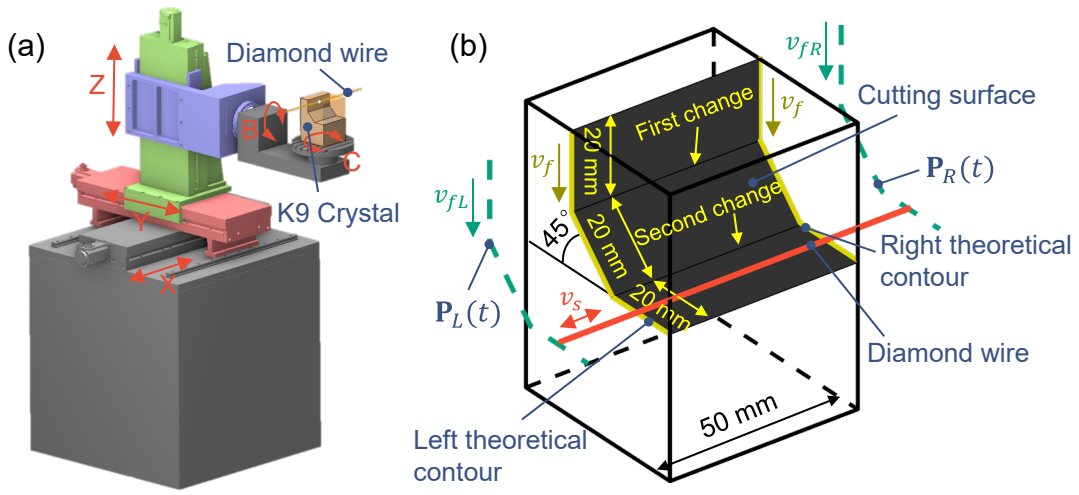

Fig. 6. Experimental design of wire sawing curved surface (a) and cutting trajectory (b). (Workpiece is mounted on a five-axis CNC machine, and material removal is achieved by controlling the movements along the X, Y, and Z axes and the rotation of the B and C axes to bring the workpiece into contact with the wire).

During machining, the workpiece feed rate v_f represents the average rate of movement of the workpiece. This was equivalent to the average feed rate of the theoretical contour lines on both sides of the target workpiece (indicated by the yellow line in **Fig. 6b**). The workpiece feed rate v_f and time interval *dt* were set to obtain the $\mathbf{P}_L$ and $\mathbf{P}_R$ control path points at both ends of the wire using inverse kinematic calculations. The wire was obtained at both end feed rates, v_{fL} and v_{fR}.

The wire moved back and forth between the two spools at a velocity v_s, periodically reversing its direction. A complete reciprocating cycle comprised six stages, as shown in **Fig. 7**. Reciprocating cycle time T_s=120 s and acceleration a_s=2 m/s^2.

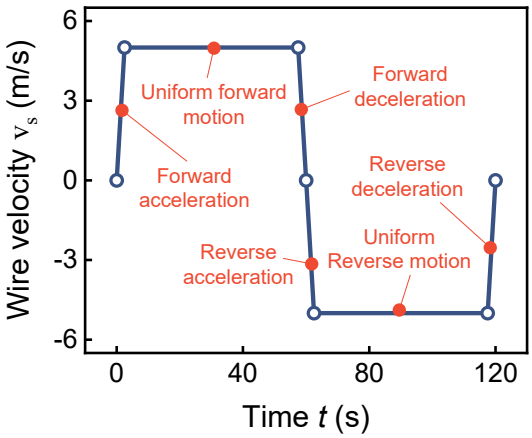

Fig. 7. Complete reciprocating cycle movement of the diamond wire. (A complete reciprocating cycle of the wire includes six stages, forward acceleration, uniform forward motion, forward deceleration, reverse acceleration, uniform reverse motion and reverse deceleration).

3.2. Measurement of wire bow angle

The wire bow angle measuring device for the curved DWS surface is shown in **Fig. 8.** The wire bow angle measuring device consists of two spring displacement sensors installed perpendicularly to each other. The deformation values of the wire were based on the mathematical relationship between the output voltage and the displacement of the telescopic rod. The wire bow angle calculation formula was used to compute the changes in the wire bow angle.

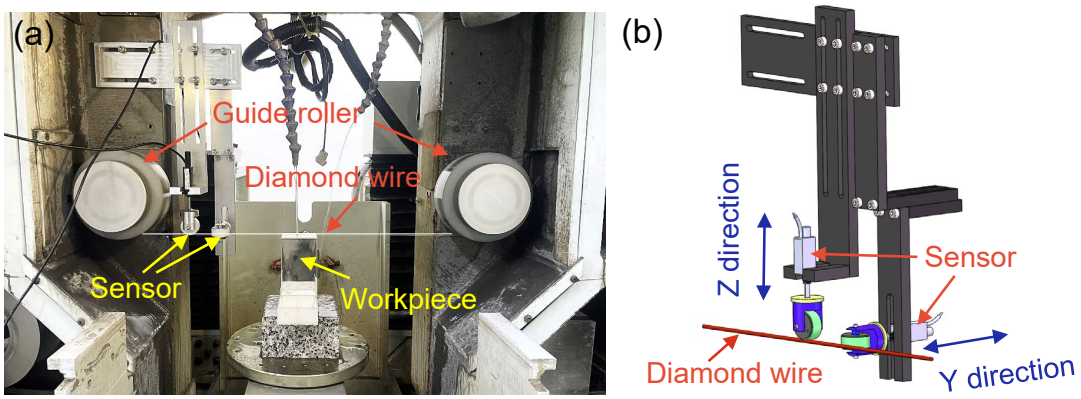

Fig. 8. Construction design (a) and theoretical schematic (b) of the wire bow angle measurement for diamond wire sawing on curved surface. (Spring displacement sensors are installed perpendicular to each other, and wire bow angle is obtained through the displacement).

The wire bow angle on both sides was defined as the angle between the wire outside the workpiece and the theoretical straight line inside the workpiece. The wire bow angle was calculated using **Eq. (20).**

$$\begin{aligned}\theta_{bowL} &= \arccos\left(\frac{\boldsymbol{W_1W_2}\cdot\boldsymbol{W_2W_{M-1}}}{\left|\boldsymbol{W_1W_2}\right|\cdot\left|\boldsymbol{W_2W_{M-1}}\right|}\right)\\ \theta_{bowR} &= \arccos\left(\frac{\boldsymbol{W_{M-1}W_M}\cdot\boldsymbol{W_2W_{M-1}}}{\left|\boldsymbol{W_{M-1}W_M}\right|\cdot\left|\boldsymbol{W_2W_{M-1}}\right|}\right)\end{aligned}, \tag{19}$$

where $\theta_{bowL,R}$is the wire bow angle on both sides of the workpiece.

3.3. Comparison between simulation and experimental results

The simulated results in terms of the wire bow angle for DWS on the curved surface were calculated using a trial-and-error method under different Preston coefficients. The results showed that when the Preston coefficient was 7.4×10^{-5} mm^2/N, the maximum error between the experimental and simulation results was minimized. Therefore, the value of $k_f$was set to 7.4×10^{-5} mm^2/N in the simulation. The force ratio coefficient μ for cutting K9 crystal with a wire is 0.5 [72]. Furthermore, the initial horizontal interval between contact points *dx* was set to 0.1 mm, and the time interval *dt* was set to 0.01 s during calculation. The other simulation and experimental parameters are listed in **Table 1.**

Table 1. Parameters of simulation and experiment

Parameter	Symbol	Numerical value
Workpiece feed rate	v_f	0.5 mm/min
Workpiece length	L_W	50 mm
Preloading force	F_1	30 N
Distance between two rollers	L	486 mm
Cutting fluid flow rate	V	0.5 L/min
Max wire velocity	v_{max}	5 m/s
Wire motion acceleration	a_w	2 m/s^2
Wire reciprocating cycle time	T_s	120 s
Wire diameter	d_w	250 μm
Diamond grit size on the wire	d_m	30-40 μm
Diamond grit number on the wire	d_{num}	10-16 grits/mm
Time intervals	dt	0.01 s
Initial horizontal interval	dx	0.1 mm
Force ratio coefficient	μ	0.5
Preston coefficient	k_f	7.4×10^{-5} mm^2/N
The influence of preloading force on simulation results	F_1	30; 35; 40; 45; 50 N
The influence of max wire velocity on simulation results	v_{max}	5; 10; 15; 20; 25 m/s
The influence of workpiece feed rate on simulation results	v_f	0.2; 0.3; 0.4; 0.5; 0.6 mm/min

A comparison of the wire bow angles between the experimental measurements and simulation results is shown in **Fig. 9**. The comparison demonstrates a strong agreement between the wire bow angles calculated through the simulation and the experimental measurements, with a maximum error value of less than 0.17°.

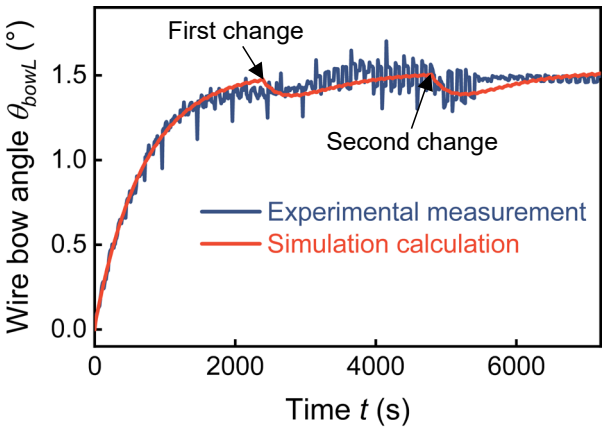

Fig. 9. Comparison of wide bow angle: experimental measurement results versus simulation calculation results in curved surface cutting process.

The results of the experimental measurements and simulations reveal a consistent trend in the wire bow angle during the sawing process. Initially, the wire bow angle increased before leveling off, with a diminishing rate of increase over time. When the direction of the sawing motion changed, the wire bow angle first decreased, then increased, and eventually stabilized. In the stable state, the wire bow angles were essentially the same. Changes in the sawing motion direction had a relatively insignificant effect on the experimental results for the wire bow angle.

4. Mechanical model simulation of curved surface wire sawing

4.1. Effect of machining twist surface on the simulation results of wire bow angle

Curved surface models for DWS are typically constructed using the ruled surface model. Xu et al. [20] introduced a layer envelope splicing fitting method to construct a ruled surface model that enables the constructed model to twist along the layered direction, thereby enhancing the material removal rate. In this study, a mechanical simulation model for a curved surface is proposed to analyze the impact of a machined, twisted surface on the wire bow angle. The sawing trajectories of the machined twisted and non-twisted surfaces are shown in **Fig. 10.**

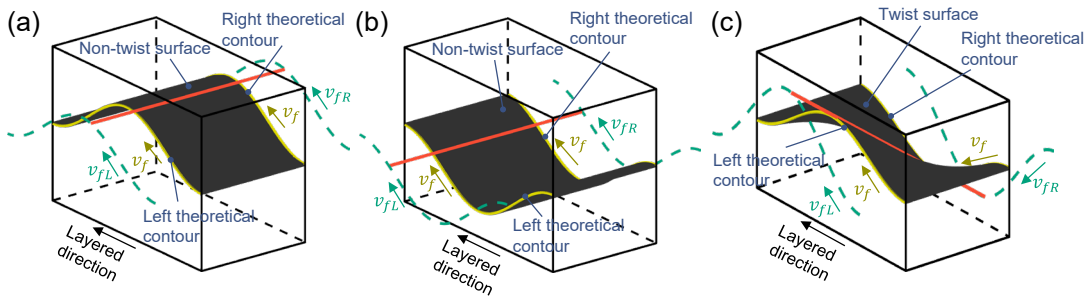

Fig. 10. Schematic of sawing trajectory of twist surface machining (c) and its comparison object non-twist surface machining (a) and (b). ((c) simulated machining process of a twist surface where the machining motion direction on both sides is opposite. The theoretical cutting contour (depicted as yellow lines) on both sides of (a) is identical to the theoretical cutting contour on the left side of (c), with the same feed rate. The theoretical cutting contour on both sides of (b) matches the theoretical cutting contour on the right side of (c), with the same feed rates).

In **Fig. 10a** and **Fig. 10b**, the simulated machining process illustrates non-twisted surfaces, serving as comparison objects for the simulated machined twisted surface shown in **Fig. 10c**. In **Fig. 10c**, the simulated machining process involves a twisted surface, showing opposite machining motion directions on both sides. The theoretical cutting contour (depicted as yellow lines) on both sides of **Fig. 10a** is identical to the theoretical cutting contour on the left side of **Fig. 10c** with the same feed rate. Similarly, the theoretical cutting contours on both sides of **Fig. 10b** match the theoretical cutting contours on the right side of **Fig. 10c** for the same feed rates. A comparison of the simulation results of the wire bow angles between the machined twisted and non-twisted surfaces is presented in **Fig. 11.**

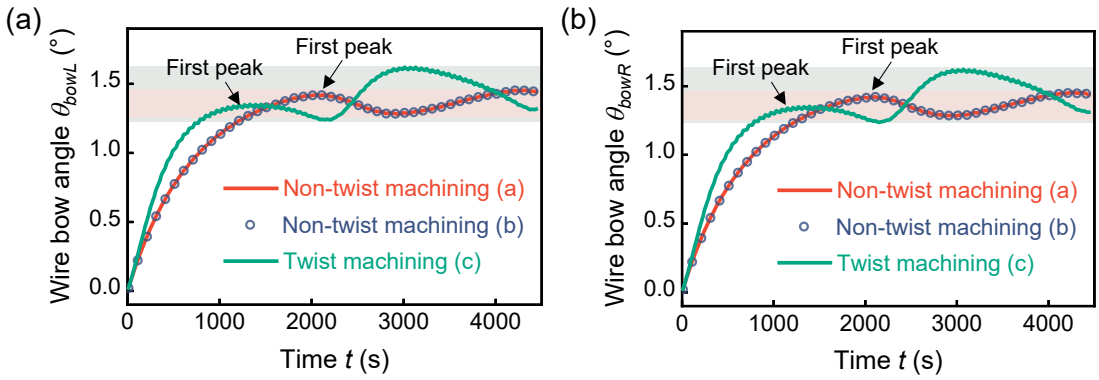

Fig. 11. Comparison of simulation results in terms of wire bow angle between the machining twist and non-twist surface. The left side (a) and the right side (b).

In non-twist surface simulation machining, the wire bow angle reached its first peak within 2200 s and maintained a relatively stable state within a certain range. The twist surface-simulating machining achieved its first peak within 1200 s. In the initial stage, the twist surface-simulating machining accelerates the rate of increase in the wire bow angle, causing it to reach its peak earlier and remain relatively stable thereafter.

During the stable state, the variation in the wire bow angle for the non-twist surface simulation machining was smaller, with a maximum value of 1.42°, a minimum value of 1.29°, and an average value of 1.36°. For the twist surface simulation machining, the wire bow angle exhibited a maximum value of 1.62°, a minimum value of 1.24°, and an average value of 1.43°. A comparative analysis of the wire bow angles during non-twist and twist surface simulation machining processes indicates that although twist surface machining increases the wire bow angle during cutting, the increase is relatively small. Moreover, twisted surface machining results in a larger float amplitude of the wire bow angle, which reduces the stability of the machining process.

During the wire-sawing simulation, the workpiece feed rate v_f represents the average rate of movement of the workpiece. This is equivalent to the average feed rate of the theoretical contour lines on both sides of the target workpiece. The feed rates at both ends of the wire, v_{fL} and v_{fR}, were calculated using a control-point set. A comparison between the wire feed rates at both ends and the wire bow angle during the twist surface-simulated sawing process is shown in **Fig. 12**.

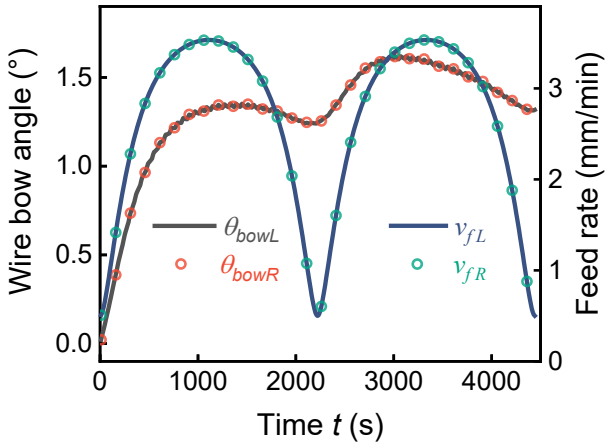

Fig. 12. Comparison of the wire feed rate at both ends and the wire bow angle during twist surface-simulating sawing process.

A comparison of the simulation results revealed that the wire bow angle on both sides of the workpiece followed a similar pattern of change when the feed rates at both ends of the wire exhibited the same pattern of change. While the workpiece feed rate remained constant, the feed rates at both ends of the wire changed over time due to the twisting motion of the wire. The variation pattern of the wire bow angle over time closely resembled that of the feed rates at both ends of the wire. This suggests that the feed rates at both ends of the wire were the primary factors influencing the change in the wire bow angle during the twisting surface-sawing process.

4.2. Effect of machining parameters on wire bow angle

Using twist surface simulation machining as an example, the influence of machining parameters on the wire bow angle was investigated during the simulation of the cutting process.

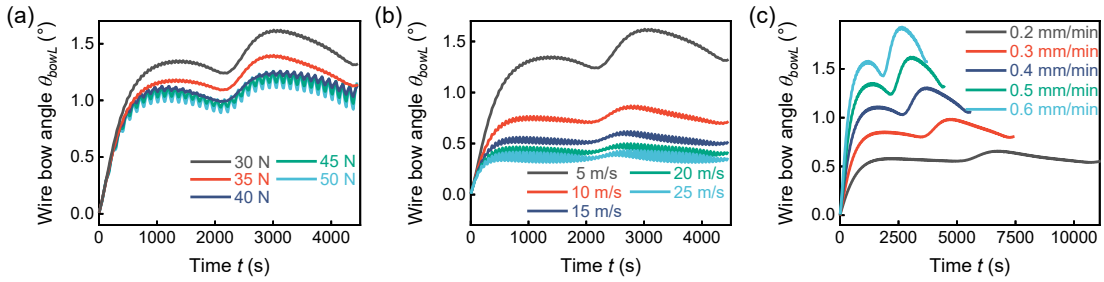

Fig. 13. Influence of different machining parameters on wire bow angle in simulating machining twist surface process. (a) Different preloading force (same max wire velocity v_{max}: 5 m/s and workpiece feed rate v_f: 0.5 mm/min), (b) different max wire velocity (same preloading force F_1: 30 N and workpiece feed rate v_f: 0.5 mm/min) and (c) different workpiece feed rate (same preloading force F_1: 30 N and max wire velocity v_{max}: 5m/s)

The impacts of various machining parameters on the wire bow angle in the twist surface-simulating machining process are shown in **Fig. 13**. A comparative analysis revealed that as the preloading force and wire velocity increased, the wire bow angle gradually decreased, and the rate of decrease gradually diminished. Conversely, an increase in the workpiece feed rate resulted in a linear increase in the wire bow angle.

Because of the continuous variation in the wire motion state throughout the simulated cutting process, the wire bow angle changed over time. Initially, the wire bow angle gradually increased before reaching a relatively stable state, where it floated within a certain range. A comparative analysis indicated that, as the wire velocity increased and the workpiece feed rate decreased, the float amplitude of the wire bow angle during the stable state decreased. Additionally, the time required for the wire bow angle to reach a stable state was reduced. This suggests that machining parameters, such as high wire velocity and low workpiece feed rate, contribute to a more stable cutting process.

A comparative analysis revealed that an increase in the preloading force and wire velocity could lead to an increase in the amplitude of periodic fluctuations caused by the reciprocating motion of the wire. This phenomenon may be owing to an increase in the preloading force, which increases the tension at each point in the transmission

process, resulting in an evident tension force difference between the entry and exit sides. Consequently, when the wire reciprocates, the amplitudes of the fluctuations on one side increase. The increase in the wire velocity prolongs the duration of the acceleration and deceleration motions while reducing the time during constant-speed motion.

5. Conclusion

This study introduced a mechanical model for wire sawing of complex curved surfaces. The model was used to analyze the interplay between the wire and workpiece, providing insights for optimizing process configurations and predicting curved surface cutting outcomes. The wire bow angle calculated through simulations exhibited strong agreement with the experimental measurements, with a maximum error value of less than 0.17°.

The influence of the twisted surface-sawing process on the wire bow angle indicated that with constant machining parameters, DWS on both twisted and non-twisted surfaces produced nearly equal average values in terms of the wire bow angle. However, the wire-twist motion increased the float amplitude of the wire bow angle. When the variation patterns of the wire feed rates at both ends were the same, the wire bow angles on both sides of the workpiece exhibited a consistent variation pattern. The wire feed rates at both ends were the primary factors influencing the change in the wire bow angle during the twist surface-sawing process.

The wire bow angle gradually decreased with increasing preloading force and wire velocity during the cutting of the twisted, curved surfaces, and the rate of decrease gradually diminished. Conversely, the wire bow angle increased linearly as the workpiece feed rate increased. Increasing the wire velocity and decreasing the workpiece feed rate can reduce the floating amplitude of the wire bow angle, thereby increasing the stability of the cutting process.

Declaration of Competing Interest

The authors declare that they have no known competing financial interests or personal relationships that could have appeared to influence the work reported in this paper.

CRediT authorship contribution statement

Zhiteng Xu: Methodology, Experiment operation, Article writing. **Xinjiang Liao:** Formal analysis, Writing-Review & Editing. **Xun Chen:** Validation, Writing-Review, Editing. **Zhiyuan Lai:** Conception of the mechanical model building. **Hui Huang:** Conceptualization, Resources, Supervision, Writing-Review & Editing.

Acknowledgements

The authors are grateful for the financial support of the National Natural Science Foundation of China (U22A20198), the Major Science and Technology Projects in Henan Province (221100230300), the Changjiang Scholars and Innovative Research Team in University (IRT_17R41), the 111 Project of China (No. B23011), and the China Scholarship Council (CSC, 202208350056).

Reference

[1] Costa EC, Xavier FA, Knoblauch R, Binder C, Weingaertner WL. Effect of cutting parameters on surface integrity of monocrystalline silicon sawn with an endless diamond wire saw. Sol Energy 2020;207:640–50. https://doi.org/10.1016/j.solener.2020.07.018.

[2] Kumar A, Melkote SN. Diamond Wire Sawing of Solar Silicon Wafers: A Sustainable Manufacturing Alternative to Loose Abrasive Slurry Sawing. Procedia Manuf 2018;21:549–66. https://doi.org/10.1016/j.promfg.2018.02.156.

[3] Gao Y, Chen Y. Sawing stress of SiC single crystal with void defect in diamond wire saw slicing. Int J Adv Manuf Technol 2019;103:1019–31. https://doi.org/10.1007/s00170-019-03579-4.

[4] Yin Y, Gao Y, Yang C. Sawing characteristics of diamond wire cutting sapphire crystal based on tool life cycle. Ceram Int 2021;47:26627–34. https://doi.org/10.1016/j.ceramint.2021.06.070.

[5] Wang N, Jiang F, Xu X, Duan N, Wen Q, Lu X. Research on the machinability of A-plane sapphire under diamond wire sawing in different sawing directions. Ceram Int 2019;45:10310–20. https://doi.org/10.1016/j.ceramint.2019.02.086.

[6] Kim H, Kim D, Kim C, Jeong H. Multi-wire sawing of sapphire crystals with reciprocating motion of electroplated diamond wires. CIRP Ann - Manuf Technol 2013;62:335–8. https://doi.org/10.1016/j.cirp.2013.03.122.

[7] Huang X, Huang H, Guo H. Simulation and Experimental Research on the Slicing Temperature of the Sapphire with Diamond Wire. Int J Comput Methods 2019;16:1–18. https://doi.org/10.1142/S021987621843003X.

[8] Zhang W, Yao C, Tang C, Qiu T, Xu X. Investigations on the trajectories of magnetic abrasive grains in magnetic induction-free abrasive wire sawing. J Magn Magn Mater 2016;419:317–24. https://doi.org/10.1016/j.jmmm.2016.06.023.

[9] Li H, Gao Y, Ge P, Bi W, Zhang L. Study on process parameters of fabrication fine diameter electroplated diamond wire for slicing crystalline silicon solar cell. Int J Adv Manuf Technol 2020;106:3153–75. https://doi.org/10.1007/s00170-019-04860-2.

[10] Chung C. Abrasive distribution of the fixed diamond wire in wire sawing process. Adv Mater Res 2012;579:145–52. https://doi.org/10.4028/www.scientific.net/AMR.579.145.

[11] Gupta A, Chen CCA, Hsu HW. Study on diamond wire wear, surface quality, and subsurface damage during multi-wire slicing of c-plane sapphire wafer. Int J Adv Manuf Technol 2019;100:1801–14. https://doi.org/10.1007/s00170-018-2656-8.

[12] Hardin CW, Qu J, Shih AJ. Fixed abrasive diamond wire saw slicing of single-crystal silicon carbide wafers. Mater Manuf Process 2004;19:355–67. https://doi.org/10.1081/AMP-120029960.

[13] Yin Y, Gao Y, Wang L, Zhang L, Pu T. Analysis of crack-free surface generation of photovoltaic polysilicon wafer cut by diamond wire saw. Sol Energy 2021;216:245–58. https://doi.org/10.1016/j.solener.2021.01.009.

[14] Costa EC, Weingaertner WL, Xavier FA. Influence of single diamond wire sawing of photovoltaic monocrystalline silicon on the feed force, surface roughness and micro-crack depth. Mater Sci Semicond Process 2022;143:106525. https://doi.org/10.1016/j.mssp.2022.106525.

[15] Gao Y, Chen Y, Ge P, Zhang L, Bi W. Study on the subsurface microcrack damage depth in electroplated diamond wire saw slicing SiC crystal. Ceram Int 2018;44:22927–34. https://doi.org/10.1016/j.ceramint.2018.09.088.

[16] Li Z, Ge P, Bi W, Li C, Wang C, Meng J. Influence of silicon anisotropy on surface shape deviation of wafer by diamond wire saw. Mater Sci Semicond Process 2021;133:105981. https://doi.org/10.1016/j.mssp.2021.105981.

[17] Wang P, Ge P, Gao Y, Bi W. Prediction of sawing force for single-crystal silicon carbide with fixed abrasive diamond wire saw. Mater Sci Semicond Process 2017;63:25–32. https://doi.org/10.1016/j.mssp.2017.01.014.

[18] Li S, Tang A, Liu Y, Wang J, Cui D, Landers RG. Analytical Force Modeling of Fixed Abrasive Diamond Wire Saw Machining with Application to SiC Monocrystal Wafer Processing. J Manuf Sci Eng Trans ASME 2017;139:1–11. https://doi.org/10.1115/1.4034792.

[19] Clark WI, Shih AJ, Hardin CW, Lemaster RL, McSpadden SB. Fixed abrasive diamond wire machining - Part I: Process monitoring and wire tension force. Int J Mach Tools Manuf 2003;43:523–32. https://doi.org/10.1016/S0890-6955(02)00215-8.

[20] Xu Z, Huang H, Cui C. Modeling and Simulation of Complex Ruled Surface Model for High Efficient Cutting with Wire Saw. Zhongguo Jixie Gongcheng/China Mech Eng 2021;32:47–53. https://doi.org/10.3969/j.issn.1004-132X.2021.01.007.

[21] Bhagavat S, Kao I. A finite element analysis of temperature variation in silicon wafers during wiresaw slicing. Int J Mach Tools Manuf 2008;48:95–106. https://doi.org/10.1016/j.ijmachtools.2007.07.009.

[22] Gao Y, Ge P, Zhang L, Bi W. Material removal and surface generation mechanisms in diamond wire sawing of silicon crystal. Mater Sci Semicond Process 2019;103:104642. https://doi.org/10.1016/j.mssp.2019.104642.

[23] Yin Y, Gao Y, Li X, Pu T, Wang L. Experimental study on slicing photovoltaic polycrystalline silicon with diamond wire saw. Mater Sci Semicond Process 2020;106:104779. https://doi.org/10.1016/j.mssp.2019.104779.

[24] Ge M, Gao Y, Ge P, Jiao Y, Bi W. A finite element analysis of sawing stress in fixed-abrasive wire saw slicing KDP crystal. Int J Adv Manuf Technol 2017;91:2049–57. https://doi.org/10.1007/s00170-016-9916-2.

[25] Möller HJ. Wafering of Silicon. Semicond Semimetals 2015;92:63–109. https://doi.org/10.1016/bs.semsem.2015.02.003.

[26] Xu Z, Huang H, Cui C, Liao X, Wu M, Xue Z. Complex-shaped metal parts high efficiency sawing with diamond wire. Int J Mech Sci 2023;250:108306. https://doi.org/10.1016/j.ijmecsci.2023.108306.

[27] Qiu J, Liu C, Li X. Evaluation method for the machining accuracy of diamond wire squaring mono-crystalline silicon and its application in comparison of reciprocating wire and endless wire. Int J Adv Manuf Technol 2022;120:1053–69. https://doi.org/10.1007/s00170-022-08865-2.

[28] Huang H, Zhang Y, Xu X. Experimental investigation on the machining characteristics of single-crystal SiC sawing with the fixed diamond wire. Int J Adv Manuf Technol 2015;81:955–65. https://doi.org/10.1007/s00170-015-7250-8.

[29] Wu H. Wire sawing technology: A state-of-the-art review. Precis Eng 2016;43:1–9. https://doi.org/10.1016/j.precisioneng.2015.08.008.

[30] Xu Z, Feng Y, Pan L, Wang X, Wang H, Jia X. Influence of ingot rocking on the surface quality of multi-wire sawing monocrystalline silicon wafers. Int J Adv Manuf Technol 2020;107:15–24. https://doi.org/10.1007/s00170-020-04996-6.

[31] Sekhar H, Fukuda T, Tanahashi K, Shirasawa K, Takato H, Ohkubo K, et al. The impact of subsurface damage on the fracture strength of diamond-wire-sawn monocrystalline silicon wafers. Jpn J Appl Phys 2018;57. https://doi.org/10.7567/JJAP.57.08RB08.

[32] Gao Y, Ge P, Hou Z. Study on removal mechanism of fixed-abrasive diamond wire saw slicing monocrystalline silicon. Key Eng Mater 2008;359–360:450–4. https://doi.org/10.4028/www.scientific.net/kem.359-360.450.

[33] Ge M, Wang P, Bi W, Ge P. Fabrication of thin resin-bonded diamond wire and its application to ductile-mode wire sawing of mono-crystalline silicon. Mater Sci Semicond Process 2021;126:105665. https://doi.org/10.1016/j.mssp.2021.105665.

[34] Yao C, Zhang W, Liu K, Li H, Peng W. A pneumatic conveying method for the manufacturing of ultraviolet curing diamond wire saws. Mater Manuf Process 2017;32:523–9. https://doi.org/10.1080/10426914.2016.1257130.

[35] Yao C, Peng W, Liu F. Formulation and implementation of energy efficient ultraviolet curing for photosensitive resin-bound diamond wire saws. Math Probl Eng 2013;2013. https://doi.org/10.1155/2013/698360.

[36] Bi W, Ge P, Gao Y, Zhu Z. Development of the manufacture equipment for resin bonded diamond abrasive wire saw. Adv Mater Res 2012;588–589:1694–7. https://doi.org/10.4028/www.scientific.net/AMR.588-589.1694.

[37] Enomoto T, Shimazaki Y, Tani Y, Suzuki M, Kanda Y. Development of a Resinoid Diamond Wire Containing Metal Powder for Slicing a Silicon Ingot. Nihon Kikai Gakkai Ronbunshu, C Hen/Transactions Japan Soc Mech Eng Part C 1999;65:1235–40. https://doi.org/10.1299/kikaic.65.1235.

[38] Pogue V, Melkote SN, Danyluk S. Residual stresses in multi-crystalline silicon photovoltaic wafers due to casting and wire sawing. Mater Sci Semicond Process 2018;75:173–82. https://doi.org/10.1016/j.mssp.2017.11.009.

[39] Yang S, Tani Y, Zhang Y, Murata J. Development of a drum-type manufacturing method for electroplated diamond wire tools. Key Eng Mater 2012;523–524:515–20. https://doi.org/10.4028/www.scientific.net/KEM.523-524.515.

[40] Albert Sun YT, Liu MC, Zhang Y, Huang YP, Chen WE. Development of an electrolyte jet type apparatus for manufacturing electroplated diamond wires. Precis Eng 2021;68:351–7. https://doi.org/10.1016/j.precisioneng.2020.12.011.

[41] Li C, Ge P, Bi W. Thermal simulation of the single discharge for electro-spark deposition diamond wire saw. Int J Adv Manuf Technol 2021;114:3597–604. https://doi.org/10.1007/s00170-021-07132-0.

[42] Yan, Xiaotong;Zuo, Dunwen;Sun, Yuli;Li, Rui;Xu Y. Manufacturing process of diamond wire saw by composite-brush-plating method. Diam Abras Eng 2017.

[43] Ge P, Gao Y, Li S, Hou Z. Study on electroplated diamond wire saw development and wire saw wear analysis. J Synth Cryst 2009;416:311–5. https://doi.org/10.4028/www.scientific.net/KEM.416.311.

[44] Chiba Y, Tani Y, Enomoto T, Sato H. Development of a high-speed manufacturing method for electroplated diamond wire tools. CIRP Ann - Manuf Technol 2003;52:281–4. https://doi.org/10.1016/S0007-8506(07)60584-8.

[45] Kamiya O, Mori H, Ito M, Takahashi M, Miyano Y, Pasang T, et al. Development of fixed grain micro-saw wire and cutting performance. Procedia Manuf 2017;13:161–8. https://doi.org/10.1016/j.promfg.2017.09.027.

[46] Zhang ZY, Xiao B, Duan DZ, Wang B, Liu SX. Investigation on the brazing mechanism and machining performance of diamond wire saw based on Cu-Sn-Ti alloy. Int J Refract Met Hard Mater 2017;66:211–9. https://doi.org/10.1016/j.ijrmhm.2017.03.010.

[47] Kamiya O , Tsuji D AF. DIAMOND AND METAL BONDING BY ACTIVE SOLDER 2006;20:3932–7.

[48] He Z, Huang H, Yin F, Xu X. Development of a brazed diamond wire for slicing single-crystal SiC ingots. Int J Adv Manuf Technol 2017;91:189–99. https://doi.org/10.1007/s00170-016-9750-6.

[49] Chung C, Van Nhat L. Generation of diamond wire sliced wafer surface based on the distribution of diamond grits. Int J Precis Eng Manuf 2014;15:789–96. https://doi.org/10.1007/s12541-014-0401-2.

[50] Teomete E. Roughness damage evolution due to wire saw process. Int J Precis Eng Manuf 2011;12:941–7. https://doi.org/10.1007/s12541-011-0126-4.

[51] Qiu J, Li X, Ge R, Liu C. Surface formation, morphology, integrity and wire marks in diamond wire slicing of mono-crystalline silicon in the photovoltaic industry. Wear 2022;488–489:204186. https://doi.org/10.1016/j.wear.2021.204186.

[52] Wang J, Jia Z, Guo YB. Shape-cutting of quartz glass by spark discharge-assisted diamond wire sawing. J Manuf Process 2018;34:131–9. https://doi.org/10.1016/j.jmapro.2018.06.001.

[53] Clark WI, Shih AJ, Lemaster RL, McSpadden SB. Fixed abrasive diamond wire machining - Part II: Experiment design and results. Int J Mach Tools Manuf 2003;43:533–42. https://doi.org/10.1016/S0890-6955(02)00216-X.

[54] Qin W, Zhidong L, Lida S, Weidong Y, Bin Z. Test research on wire deflection detection of a diamond wire saw. Int J Adv Manuf Technol 2017;91:1347–54. https://doi.org/10.1007/s00170-016-9787-6.

[55] Carton L, Riva R, Nelias D, Fourmeau M, Coustier F, Chabli A. Comparative analysis of mechanical strength of diamond-sawn silicon wafers depending on saw mark orientation, crystalline nature and thickness. Sol Energy Mater Sol Cells 2019;201:110068. https://doi.org/10.1016/j.solmat.2019.110068.

[56] Carton L, Riva R, Nélias D, Fourmeau M. Weibull strength size effect of diamond wire sawn photovoltaic silicon wafers. J Eur Ceram Soc 2020;40:5357–68. https://doi.org/10.1016/j.jeurceramsoc.2020.07.018.

[57] Wu B, Zhang Z, Feng J, Meng F, Wan S, Zhuang X, et al. Experimental Investigation on the Surface Formation Mechanism of NdFeB during Diamond Wire Sawing. Materials (Basel) 2023;16. https://doi.org/10.3390/ma16041521.

[58] Seigneur H, Schneller EJ, Shiradkar NS, Schoenfeld W V. Effect of Diamond Wire Saw Marks on Solar Cell Performance. Energy Procedia 2016;92:386–91. https://doi.org/10.1016/j.egypro.2016.07.117.

[59] Lin Z, Huang H, Xu X. Experimental and simulational investigation of wire bow deflection in single wire saw. Int J Adv Manuf Technol 2019;101:687–95. https://doi.org/10.1007/s00170-018-2919-4.

[60] Liu T, Ge P, Bi W, Gao Y. A new method of determining the slicing parameters for fixed diamond wire saw. Mater Sci Semicond Process 2020;120:105252. https://doi.org/10.1016/j.mssp.2020.105252.

[61] Teomete E. Mechanics of wire saw machining process: Experimental analyses and modeling. Iowa State Univ Diss Theses - Gradworks 2008. https://doi.org/10.13537/j.issn.1004-3918.2008.09.007.

[62] ZHANG Liaoyuan，WANG Chao，WANG Jianguang YY. Research on Cutting Trajectory of Electroplated Diamond Wire Saw. J China Ordnance 2012;8:6–10.

[63] Qiu J, Li X, Ge R, Zhang S, Wang H. Formation mechanism of wire bow and its influence on diamond wire saw process and wire cutting capability. Int J Mech Sci 2020;185. https://doi.org/10.1016/j.ijmecsci.2020.105851.

[64] Liu T, Ge P, Bi W, Gao Y. A new method of determining the slicing parameters for fixed diamond wire saw. Mater Sci Semicond Process 2020;120:105252. https://doi.org/10.1016/j.mssp.2020.105252.

[65] Liedke T, Kuna M. A macroscopic mechanical model of the wire sawing process. Int J Mach Tools Manuf 2011;51:711–20. https://doi.org/10.1016/j.ijmachtools.2011.05.005.

[66] Lai Z, Huang H, Hu Z, Liao X. Dynamic model and machining mechanism of wire sawing. J Mater Process Technol 2023;311. https://doi.org/10.1016/j.jmatprotec.2022.117820.

[67] Lu A, Jin T, Liu Q, Guo Z, Qu M, Luo H, et al. Modeling and prediction of surface topography and surface roughness in dual-axis wheel polishing of optical glass. Int J Mach Tools Manuf 2019;137:13–29. https://doi.org/10.1016/j.ijmachtools.2018.10.001.

[68] Barylski A, Piotrowski N. Non-conventional approach in single-sided lapping process: kinematic analysis and parameters optimization. Int J Adv Manuf Technol 2019;100:589–98. https://doi.org/10.1007/s00170-018-2644-z.

[69] Wang C, Yang W, Ye S, Wang Z, Yang P, Peng Y, et al. Restraint of tool path ripple based on the optimization of tool step size for sub-aperture deterministic polishing. Int J Adv Manuf Technol 2014;75:1431–8. https://doi.org/10.1007/s00170-014-6223-7.

[70] Deja M. The use of Preston equation to determine material removal during lap-grinding with electroplated CBN tools. Wear 2023;528–529:204968. https://doi.org/10.1016/j.wear.2023.204968.

[71] Zhang T, Guan C, Zhang C, Xi W, Yu T, Zhao J. Predictive modeling and experimental study of generated surface-profile for ultrasonic vibration-assisted polishing of optical glass BK7 in straight feeding process. Ceram Int 2021;47:19809–23. https://doi.org/10.1016/j.ceramint.2021.03.320.

[72] Xu Z, Huang H, Cui C. Measurement and simulation calculation of wire bow angle during the diamond wire saw process. Int J Adv Manuf Technol 2022;120:7197–204. https://doi.org/10.1007/s00170-022-09233-w.